Aerospace Science and Technology 127 (2022) 107693

Contents lists available at ScienceDirect

Aerospace Science and Technology

www.elsevier.com/locate/aescte

Development and validation of a combustion large-eddy-simulation solver based on fully compressible formulation and tabulated chemistry

Huiying Zhang [a,b], Yu Chen [a,b], Yu Lv [a,b,*]

[a] The State Key Laboratory of Nonlinear Mechanics, Institute of Mechanics, Chinese Academy of Sciences, Beijing, 100190, China
[b] School of Engineering Science, University of Chinese Academy of Sciences, Beijing, 100049, China

ARTICLE INFO

Article history:
Received 9 February 2022
Received in revised form 7 June 2022
Accepted 7 June 2022
Available online 9 June 2022
Communicated by Yongle Du

Keywords:
Compressible flow
Turbulent combustion
Large-eddy simulation
Non-premixed flame
Flamelet

ABSTRACT

This study concerns the development and validation of a high-fidelity CFD solver for large-eddy simulations (LES) of combustion and reacting flows. The solver is built upon a high-resolution numerical scheme and leverages a compressible flamelet formulation, so that it can capture both the turbulent combustion and thermoacoustic effects simultaneously. The validation study is first performed by considering a scalar-mixing case in homogeneous turbulence, and then extended to LES of a non-premixed jet flame. The solver accuracy is assessed by comparing the numerical solutions with the available experimental data. It is found that the newly developed solver is able to accurately predict the time-averaged combustion fields as well as the fluctuation quantities. The predictive accuracy is comparable to that of the state-of-the-art low-Mach solvers in literature.

1. Introduction

Numerical simulation is a vital tool for performance assessment and design optimization of aero-propulsion devices, in which the key physical process is combustion. Based on the fidelity, the numerical simulations may be categorized to three types: direct numerical simulation (DNS), large-eddy simulation (LES), and Reynolds-Averaged Naiver-Stokes (RANS) equations simulation. Due to the nowadays computing power limit, DNS remains unaffordable for practically-relevance combustion applications. Meanwhile, RANS which contains a number of empirical parameters requires parameter tuning and only works well for very limited flame configuration. As one of the most promising alternative [1], LES has gained remarkable progress in combustion modeling, and been widely used in simulations of premixed [2–5] and non-premixed flames [6,7].

Several models have been established for combustion LES: steady and unsteady flamelet models [8], thickened flame model [9], transported FDF models [10–12], conditional momentum closure [13,14] and others. Among those models, the flamelet approach has its advantages thanks to the simply formulation, superior computational efficiency, and the ability of employing complex chemical mechanisms, and thereby been adopted broadly in combustion LES for both academic studies and industrial applications. Also, research efforts have over the years led to different variants and extensions of flamelet models. Pierce and Moin [15] proposed to use the progress variable instead of the scalar dissipation rate, which is known as flamelet/progress variable model (FPV) and now widely used in the non-premixed flame predictions. Pitsch and Ihme [16] extended the steady model by considering the unsteadiness of the flame structure. To predict flame extinction and reignition, a statistically most likely distribution of conserved and reactive scalars is later proposed [17,18]. From the mathematical point of view, the flamelet model provides a low-order manifold of thermochemical states that relate density, temperature, species mass fractions, and thermal and transport properties. Algorithmically, these low-order representations (flamelets) are generated efficiently by solving flamelet equations (or the equivalence, such as one-dimensional or axisymmetric flame problems), and the thermochemical states are tabulated as functions of a small set of variables. Despite few exceptions, flamelet models were implemented mostly in low-Mach solvers that can handle variable-density flows. These solvers include commercial solvers such as Ansys Fluent, open-source platforms such as OpenFOAM, and academic codes such as NGA.

In spite of the significant success, the low-Mach flamelet formulation has its inherent limitations. First of all, it is not appli-

* Corresponding author at: The State Key Laboratory of Nonlinear Mechanics, Institute of Mechanics, Chinese Academy of Sciences, Beijing, 100190, China.
E-mail address: lvyu@imech.ac.cn (Y. Lv).

https://doi.org/10.1016/j.ast.2022.107693
1270-9638/

cable to the combustion processes with high-speed flow streams, for example, the scramjet combustion configuration [19–21]. Secondly, it precludes the direct predictions and simulations of the acoustic and flame interaction for the study of thermoacoustic instability [5,22]. There is a need to extend the flamelet model to compressible formulation. The extensions of the model to the compressible flows [23–26] have been made over recent years. However, the efforts were focused primarily on supersonic combustion configurations, such as the bluff body combustion [23], and the suitability and accuracy of the holistic modeling framework in applications to low-Mach or intermediately compressible flow regimes require further assessment. To address these need, we develop and validate a new combustion LES solver in this study, with the goal to continue evaluating the capability of compressible flamelet model. Our ultimate objective is to study combustion instability and thermoacoustics. To this end, a combustion solver based on compressible formulation and efficient combustion model shall be developed and validated. This work will serve as a stepping stone for further advancing our combustion-modeling capabilities.

The rest of the paper is structured as follows. Section 2 introduces the model formulation and the numerical method, followed by the numerical test performed in Section 3 with consideration of a scalar-mixing case in homogeneous turbulence. Thereafter, we focus on the comprehensive validation study in Section 4 and the Sandia Flame D case is used as the benchmark case. The LES predictions of velocity and scalar fields are compared against the experimental measurements and the mesh sensitivity is also assessed. Lastly, the study finished with the conclusions in Section 5.

2. Solution techniques

In this section, we state the mathematical formulations, including the governing equations and the specific combustion model, followed by the numerical methods.

2.1. Governing equations

As discussed in the introduction, we target the combustion problems with compressible flow formulation. For this, the filtered Navier-Stokes equations with consideration of relevant scalars are solved. The governing equations in the fully conservation form read:

$$\frac{\partial \bar{\rho}}{\partial t} + \frac{\partial \bar{\rho}\tilde{u_j}}{\partial x_j} = 0\,, \tag{1}$$

$$\frac{\partial \bar{\rho}\tilde{u}_i}{\partial t} + \frac{\partial \bar{\rho}\tilde{u}_i\tilde{u}_j}{\partial x_j} = -\frac{\partial \bar{p}}{\partial x_i} + \frac{\partial \bar{\tau}_{ji}}{\partial x_j} + \frac{\partial \tau_{ji}^{sgs}}{\partial x_j}\,, \tag{2}$$

$$\frac{\partial \bar{\rho}\tilde{E}}{\partial t} + \frac{\partial \bar{\rho}\tilde{E}\tilde{u}_j}{\partial x_j} = -\frac{\partial \bar{p}\tilde{u}_j}{\partial x_j} + \frac{\partial \bar{\tau}_{ji}\tilde{u_i}}{\partial x_j} - \frac{\partial \bar{q}_j}{\partial x_j} + \frac{\partial \psi_{e,j}^{sgs}}{\partial x_j} + \tilde{u}_i\frac{\partial \tau_{ji}^{sgs}}{\partial x_j}\,, \tag{3}$$

$$\frac{\partial \bar{\rho}\tilde{Y}_\alpha}{\partial t} + \frac{\partial \bar{\rho}\tilde{u}_j\tilde{Y}_\alpha}{\partial x_j} = \frac{\partial}{\partial x_j}(\bar{\rho}D_\alpha\frac{\partial \tilde{Y}_\alpha}{\partial x_j}) + \frac{\partial \psi_{Y,j}^{sgs}}{\partial x_j} + \bar{\dot{\omega}}_\alpha, \tag{4}$$

in which $\bar{\rho}$ and $\bar{p}$ are the Reynolds-filtered density and pressure, and $\tilde{u}$, $\tilde{E}$, and $\tilde{Y}_\alpha$ are Favre-filtered velocity, total energy and species mass fraction, respectively. The total energy takes the form of $\tilde{E} = \tilde{e} + \widetilde{u_k^2}/2$, in which e denotes the internal energy with both the sensible and chemical contributions. $\bar{\tau}_{ij}$ is the Reynolds-filtered stress tensor while $\bar{q}_j$ represents the conductive heat flux. The subgrid-scale terms are indicated via the superscript "sgs", and these terms are modeled by invoking the eddy-viscosity assumption:

$$\tau_{ij}^{sgs} = \bar{\rho}\tilde{u}_i\tilde{u}_j - \bar{\rho}\widetilde{u_iu_j} \approx \mu_t\left(\frac{\partial \bar{u}_j}{\partial x_i} + \frac{\partial \bar{u}_i}{\partial x_j}\right)\,, \tag{5a}$$

$$\psi_{Y,j}^{sgs} = \bar{\rho}\tilde{u}_i\tilde{Y}_\alpha - \bar{\rho}\widetilde{u_iY_\alpha} \approx \rho D_t\frac{\partial \tilde{Y}_\alpha}{\partial x_j}\,, \tag{5b}$$

$$\psi_{e,j}^{sgs} \approx \bar{\rho}\tilde{h}\tilde{u}_j - \bar{\rho}\widetilde{hu}_j \approx \kappa_t\frac{\partial \tilde{T}_j}{\partial x_j}\,, \tag{5c}$$

in which μ_t, D_t and κ_t are the eddy viscosity, the eddy diffusivity, and the eddy thermal conductivity, respectively. They are related through the turbulent Schmidt number $\mathrm{Sc}_t = \mu_t/(\rho D_t)$ and the turbulent Prandtl number $\mathrm{Pr}_t = c_p\mu_t/\kappa_t$, where c_p is the heat capacity at constant pressure. In this study, we employ the Vreman model [27] to formulate the eddy viscosity, μ_t, and Sc_t and Pr_t are both set to 0.9. It is worth noting that the central question of combustion LES is to develop closure model for the filtered chemical source term $\bar{\dot{\omega}}_\alpha$ in Eq. (4).

2.2. Compressible flamelet/progress variable (CFPV) model

In this study, we employ the compressible version of flamelet/progress variable model [23]. For this, we first state the classical FPV model and then discuss its extension to the compressible flow formulation. For combustion with high Damköhler number, the flamelet model commonly assumes that the chemical reaction time-scale is faster than the turbulent time scales and hence the turbulent eddies do not disrupt the inherent laminar flame structure. Under this model assumption, any thermochemical quantity may be expressed as a function of the mixture fraction Z and a progress variable C:

$$\phi = \phi(Z,\ C)\,, \tag{6}$$

in which C is often defined as a linear combination of combustion products. Fig. 1 shows the flamelets generated under various scalar dissipation rates, χ, for Sanida Flame D. Note that $\chi = 2D_Z|\nabla Z|$ is a controlling parameter which represents the effect of local flow strain on the flame. The parameterization of thermochemical states is illustrated in Fig. 1 (b).

In the context of LES, the tabulation must take the filtering effect into account. In the model proposed by Piece and Moin [15], the filtered thermochemical states are correlated statistically with the mixture fraction and the progress variable by a presumed joint PDF–$\beta(Z;\ \tilde{Z},\ \widetilde{Z''^2})\delta(C-\tilde{C})$. This means that the thermochemical states follow a *beta*-distribution of Z, depending on the filtered mixture fraction $\tilde{Z}$ and the filtered mixture-fraction variance $\widetilde{Z''^2}$, and a *delta*-distribution of C, depending on the filtered progress variable $\tilde{C}$. Finally, each filtered quantity is calculated via the convolution and parameterized in the following form,

$$\tilde{\phi} = \int\int \phi(Z,\ C)\beta(Z;\ \tilde{Z},\ \widetilde{Z''^2})\delta(C-\tilde{C})dZdC = \tilde{\phi}(\tilde{Z},\ \tilde{C},\ \widetilde{Z''^2})\,, \tag{7}$$

which is then stored in a three-dimensional chemical library. From the mathematical point of view, $\tilde{Z}$, $\tilde{C}$ and $\widetilde{Z''^2}$ now serve as the independent variables instead of all the species concentrations which could be in a large number. Therefore, Eqs. (4) are no longer parts of the governing equations, and the following three equations are substituted:

$$\frac{\partial \bar{\rho}\tilde{Z}}{\partial t} + \frac{\partial \bar{\rho}\tilde{u}_j\tilde{Z}}{\partial x_j} = \frac{\partial}{\partial x_j}(\bar{\rho}D_Z\frac{\partial \tilde{Z}}{\partial x_j}) + \frac{\partial \psi_{Z,j}^{sgs}}{\partial x_j}\,, \tag{8}$$

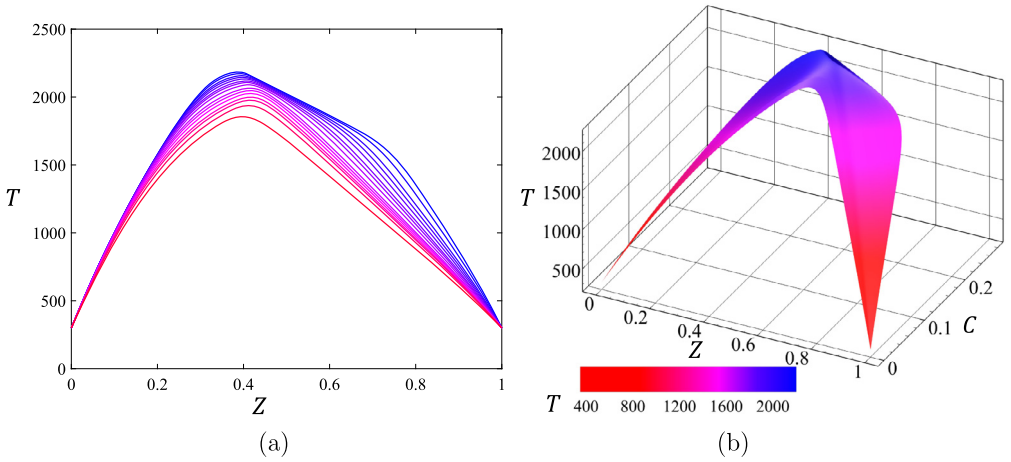

Fig. 1. Flamelet solutions obtained for the Sandia Flame D case: (a) temperature profiles for various χ values; and (b) temperature profiles in (Z, C) space. (For interpretation of the colors in the figure(s), the reader is referred to the web version of this article.)

$$\frac{\bar{\rho}\widetilde{Z''^2}}{\partial t} + \frac{\partial \bar{\rho}\tilde{u}_j\widetilde{Z''^2}}{\partial x_j} = \frac{\partial}{\partial x_j}(\bar{\rho}D_Z\frac{\partial \widetilde{Z''^2}}{\partial x_j}) + \frac{\partial \psi^{sgs}_{Z''^2,j}}{\partial x_j} + 2\frac{\mu_t}{\mathrm{Sc}_t}\frac{\partial \tilde{Z}}{\partial x_j}\frac{\partial \tilde{Z}}{\partial x_j} - \bar{\rho}\tilde{\chi}, \tag{9}$$

$$\frac{\partial \bar{\rho}\tilde{C}}{\partial t} + \frac{\partial \bar{\rho}\tilde{u}_j\tilde{C}}{\partial x_j} = \frac{\partial}{\partial x_j}(\bar{\rho}D_C\frac{\partial \tilde{C}}{\partial x_j}) + \frac{\partial \psi^{sgs}_{C,j}}{\partial x_j} + \bar{\dot{\omega}}_C, \tag{10}$$

in which the subgrid transport terms are modeled using the gradient-based eddy-viscosity formulation similar to Eq. (5b). The laminar diffusivity is evaluated as $D_Z = D_C = \tilde{\mu}/(\bar{\rho}\mathrm{Sc})$, where the laminar viscosity is checked out from the chemical library and the laminar Schmidt number, Sc, is set to 0.7.

It should be aware that the governing equations are still unclosed, as a procedure for pressure evaluation is required. In the low-Mach formulation, the pressure is obtained naturally via the Poisson equations that enforce the continuity equation considering the variable density. However, for the compressible formulation pressure should be associated with the energy and the equation of state, and an new evaluation procedure is required. For this, we resort to the following relation of internal energy:

$$\tilde{e} = \tilde{e}_0 + \int_{T_0}^{\tilde{T}} \tilde{c}_v(T)dT \approx \tilde{e}_0 + \int_{T_0}^{\tilde{T}} \frac{\tilde{R}}{\tilde{\gamma}(T)-1}dT\,, \tag{11}$$

where the quantities with the "0" subscript refer to those in the table obtained at the baseline pressure. The temperature dependence of thermal property is treated through a linear expansion:

$$\tilde{\gamma}(T) = \tilde{\gamma}_0 + a_\gamma(T - T_0)\,, \tag{12}$$

with which the temperature and energy is related analytically with integral-free formulas:

$$\tilde{e} = \tilde{e}_0 + \frac{\tilde{R}}{\alpha_\gamma} ln(1 + \frac{a_\gamma(\tilde{T} - T_0)}{\tilde{\gamma}_0} - 1)\,, \tag{13}$$

and

$$\tilde{T} = T_0 + \frac{\tilde{\gamma}_0 - 1}{a_\gamma}(e^{a_\gamma(\tilde{e}-\tilde{e}_0)/\tilde{R}} - 1)\,. \tag{14}$$

After the temperature is obtained, the equation of state of the ideal gas is employed to evaluate the pressure:

$$\bar{p} = \bar{\rho}\widetilde{RT} \approx \bar{\rho}\tilde{R}\tilde{T}\,, \tag{15}$$

under the assumption that $\widetilde{RT} \approx \tilde{R}\tilde{T}$ [28,29]. The values of $\tilde{e}_0$, $\tilde{R}_0$, $\tilde{\gamma}_0$, T_0 and α_γ can be computed during a pre-processing step and tabulated in the flamelet library. It is noteworthy that the above model procedure for pressure evaluation does not require an Newton iterative step to invert the temperature as a function of energy, and therefore is more efficient and robust. Moreover, the present study focuses on testing the compressible flamelet model in the subsonic flow region which does not involve strong pressure variations due to shock or expansion. The mixture composition is not affected by the compressibility and thereby considered frozen at the baseline condition:

$$\tilde{Y}_i \approx \tilde{Y}_{i,0}(\tilde{Z},\ \tilde{C},\ \widetilde{Z''^2}), \quad \tilde{R} \approx \tilde{R}_0(\tilde{Z},\ \tilde{C},\ \widetilde{Z''^2})\,. \tag{16}$$

Meanwhile, other quantities of interest can be obtained via the 1st-order Taylor expansion:

$$\tilde{\phi} \approx \tilde{\phi}_0 + \left(c_v\frac{d\phi}{de}\right)\Big|_0(\tilde{T} - T_0)\,. \tag{17}$$

The linearization coefficient (derivative) can be generated by perturbing the baseline flamelet solution and examining the change of the corresponding quantity. It can also be pre-computed and stored in the flamelet library.

It is worthwhile to clarify the difference between compressible and standard FPVs. In standard FPV, the energy equation is not solved and the pressure is obtained from the Poisson equation with the consideration of variable density. In compressible FPV in which energy equation must be solved, the pressure should be evaluated based on energy, density, and tabulated thermodynamic properties. In this study, we rely on a linearized thermal property relation (see Eq. (12)) to obtain temperature (see Eq. (14)) and then pressure (see Eqs. (15)). In FPV-based studies of supersonic combustion, researchers often employ pressure-corrected chemical source terms. In our study, the pressure fluctuation is negligible and therefore that correction is not included.

Now the effort is taken to generate the flamelets that represent the functional relation of Eq. (6). For this, the steady flamelet equations [8,28] are solved using the FlameMaster code [30]. The chemistry for methane/air combustion is described using the GRI-mech 3.0 chemical mechanism, consisting of 53 species and 325 elementary reaction steps. The boundary conditions on the fuel and oxidizer sides, including composition and temperature, are prescribed according to the specific flame configuration given in

Section 4.1. The baseline pressure is set to 1 atm in this work. In the present work, the progress variable is defined as $C = Y_{CO_2} + Y_{CO} + Y_{H_2O} + Y_{H_2}$.

2.3. Numerical methods

The computational capability used in this study is built upon our previous numerical development efforts and implemented in SUPES (Scalable mUlti-Physics Entropy-Stable) solver [31]. The reconstruction based on finite-volume scheme [32] is employed. The specific algorithm is following:

- In each cell, construct a $\mathcal{P}^k$ polynomial (k refers to polynomial order) with C_1 natural neighbors. For a hexahedral cell with six neighbors, a quadratic polynomial, $\mathcal{P}^2$, with a set of basis functions $\{1,\ x,\ y,\ z,\ x^2,\ y^2,\ z^2\}$ can be constructed, while for a tetrahedral cell with four neighbors, a linear polynomial, $\mathcal{P}^1$, with basis functions $\{1,\ x,\ y,\ z\}$ can be constructed.
- On each edge, interpolate the polynomials in the left and right cells onto a set of surface quadrature point and evaluate the summation of Riemann flux (here we use a blend formulation: central/AUSM+ [33]) via a Gauss quadrature.
- In each cell, once the residual, **R**, is assembled the cell solution, **U**, is updated with a strong-stability preserving 3rd-order Runge-Kutta time-integration scheme:

$$\mathbf{U}^{(1)} = \mathbf{U}^n + \Delta t \mathbf{R}\left(\mathbf{U}^n\right) , \tag{18a}$$

$$\mathbf{U}^{(2)} = \frac{3}{4}\mathbf{U}^n + \frac{1}{4}\left(\mathbf{U}^{(1)} + \Delta t \mathbf{R}(\mathbf{U}^{(1)})\right) , \tag{18b}$$

$$\mathbf{U}^{n+1} = \frac{1}{3}\mathbf{U}^n + \frac{2}{3}\left(\mathbf{U}^{(2)} + \Delta t \mathbf{R}(\mathbf{U}^{(2)})\right) . \tag{18c}$$

Since SUPES already has a discontinuous Galerkin framework [34–36,31], the above finite-volume implementation can be enabled straightforwardly in the existing infrastructure. Moreover, the numerical method provides a guaranteed 2nd-order accuracy, while hexahedral cells are preferred as the quadratic reconstruction can be employed.

3. Numerical test

To test the developed capability for LES with multi-components, we first consider a non-reactive scalar mixing case for verification. An idealized setting is utilized, in which two scalars diffuse into each other in a three-dimensional box initialized with an isotropic turbulent field. The initial velocity field is generated using a pseudos-turbulence spectrum:

$$E_u(k) = 16\sqrt{\frac{2}{\pi}}u'^2\frac{k^4}{k_0^5}\exp(-\frac{2k^2}{k_0^2}) , \tag{19}$$

in which k_0 is the most energetic wavenumber associated with the Taylor microscale λ and u' is the velocity fluctuation intensity. In this case, the Reynolds number at the Taylor scale, $\mathrm{Re}_\lambda = u'\lambda/\nu$, is set to 100; and the turbulent Mach number, $\mathrm{Ma}_t = \sqrt{3}u'/c$, is set to 0.1. Accordingly, the initial pressure and density fields are then prescribed. The passive scalar field is generated following the Eswaran & Pope's approach [37] and illustrated in Fig. 2. It should be noted that the mean flow is zero in this case. Compressible formulation introduces numerical dissipation which scales with the characteristic wave speed with the maximum absolute value. In subsonic regime, the specific absolute value could be $|u + c|$ or $|u - c|$. Since Mach number is less than one everywhere in this case, both $|u + c|$ and $|u - c|$ are guaranteed to be non-zero and the corresponding characteristic directions are always well-defined. Therefore, the numerical stability is achieved.

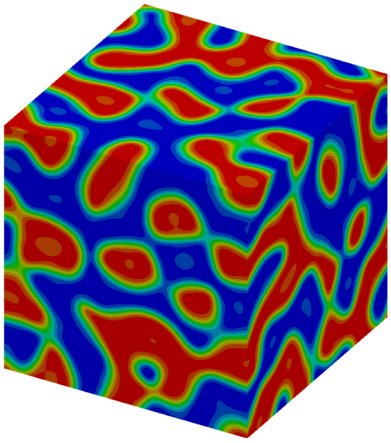

Fig. 2. Initial scalar field of the mixing case.

In this part, we first carry out the direct numerical simulation with 256^3 cells to generate the reference results. Then, the verification on the LES is performed at different mesh resolutions–64^3, 32^3, and 16^3 cells, with the corresponding filtered initial conditions. For each LES case, we sample the turbulent kinetic energy and scalar energy in time, which are then compared with the filtered DNS reference results. As shown in Fig. 3, the filtered DNS results are well replicated by the LES calculations at all mesh resolutions considered. Hence, it is shown that the developed LES framework is able to deliver robust predictions for non-reactive flows with consideration of scalar mixing, setting the foundation for reacting flow simulations.

4. Validation study – LES of Sandia Flame D

4.1. Flame configuration and computational setup

The Sandia flame experiments were experimentally studied by Barlow et al. [38,39] and Scheider et al. [40]. The piloted coaxial methane-air jet flame (Sandia Flame D) is characterized by three inlet streams. The fuel, consisting of 25% methane and 75% air by volume, is issued through the main jet. The jet diameter, D, is 0.0072 m and the bulk velocity equals to 49.6 m/s, and the related Reynolds number is 22,400. The fluid of the pilot jet is a lean ($\Phi = 0.77$) mixture of C_2H_2, H_2, air, CO_2 and N_2, which has the same nominal enthalpy and equilibrium composition as methane/air at the same equivalence ratio. The out diameter of the annular pilot stream is $2.53D$ and the velocity of pilot gas is 11.4 m/s. The coflow velocity is 0.9 m/s.

In our numerical study, the computational domain is set to $x \times y \times z = 80D \times 26.5D \times 2\pi$, where x, y and z, respectively, represent the axial, radial, and circumferential directions. Two meshes are considered: a coarse mesh with 1.4 million cells and a fine mesh with 3.9 million cells. Fig. 4(a) shows the fine mesh in the $z = 0$ plane. The mesh is refined near the inlet and the centerline of the computational domain, as illustrated in a cross-section cut along the x-direction in Fig. 4(b). Fig. 4(c) gives the zoom-in view near the fuel nozzle. To accurately represent the jet turbulence, an inflow turbulence boundary condition is required. For this, we employ the digital-filter based method [41–43] to generate the inflow turbulence and apply it at the inlet of main jet. The adiabatic boundary condition is utilized for the nozzle walls as well as the side walls, and the outflow boundary is prescribed as a pressure outlet with the fixed pressure value of 1 atm.

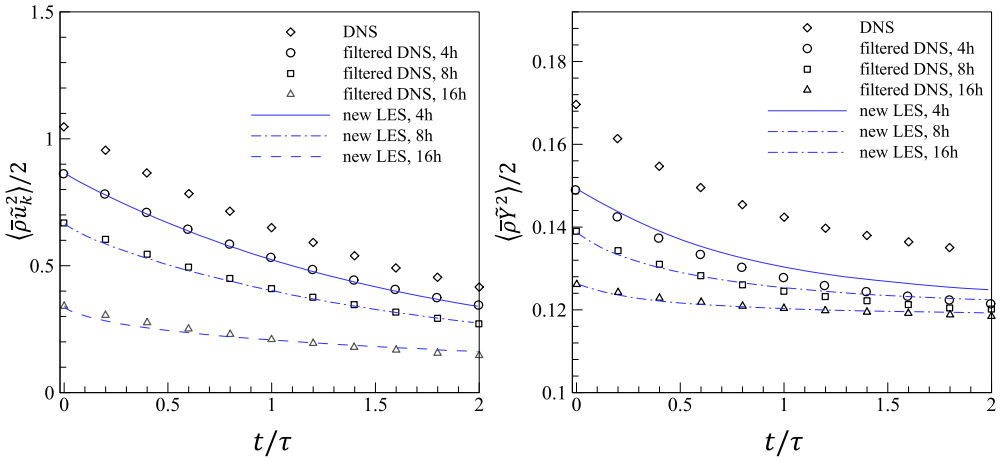

Fig. 3. Comparison of the LES predicted turbulent kinetic energy (left) and the scalar energy (right) with the filtered DNS results.

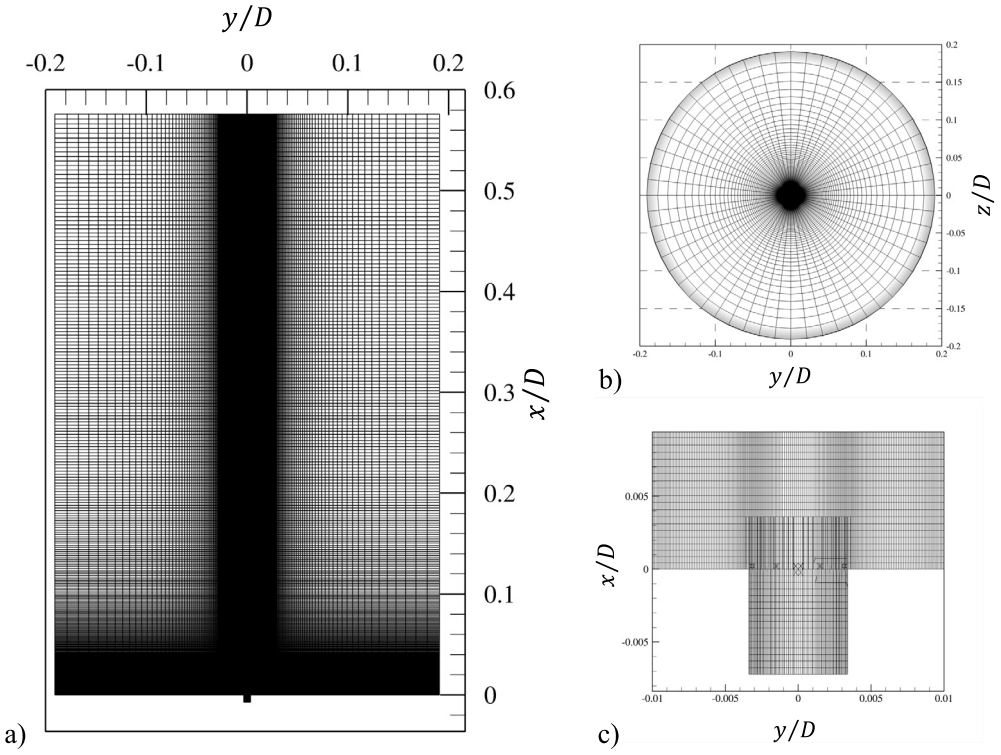

Fig. 4. a) Computational fine mesh in the $x-y$ plane, b) computational mesh at the inlet plane of the fuel nozzle, and c) zoom-in view of Fig. 4 a) near the inlet of fuel nozzle.

4.2. Results

In this section, we assess the LES results through the comparison against the experiment data and the previously reported LES results. Also, the LES predictions on two different meshes are compared.

Fig. 5 shows the predicted instantaneous temperature and streamwise velocity fields of Sandia Flame D. The flame is anchored upon the pilot and the flame front emerges in the mixing layer between the high-speed fuel jet and slow surrounding gases, as illustrated in the temperature field of Fig. 5(a). Near the inlet the flame modulation by large coherent structure is observed, while toward the downstream the flame gradually turns to be a fully turbulent mode. Along the axial direction, the increased reaction intensity contributes to the ascending trend of the temperature. The flame fronts around the jet merge at $x = 30 \sim 40D$, where the maximum temperature about 2100 K is observed. After reaching the peak temperature, the temperature drops sharply. As for the velocity, it is shown in Fig. 5(b) that the jet slows down axially while expands radially because of the mixing with the quiescent surrounding air. Moreover, as the combustion leads to enlarged viscosity, the jet of reacting flow is more elongated with slower velocity decay along the axial direction, as compared to the conventional cold jet. There is no intense breakup of potential core.

Fig. 6 shows the LES predicted time-average and root-mean-square (rms) temperature, along with the measurement data [38, 39], at different axial locations. Each radial axis is normalized by the corresponding axial distance. It is observed in Fig. 6(a) that the mean temperature profiles compare well with the experimental data. The peak mean temperature predicted by our solver is slightly closer to the centerline. The centerline temperature ex-

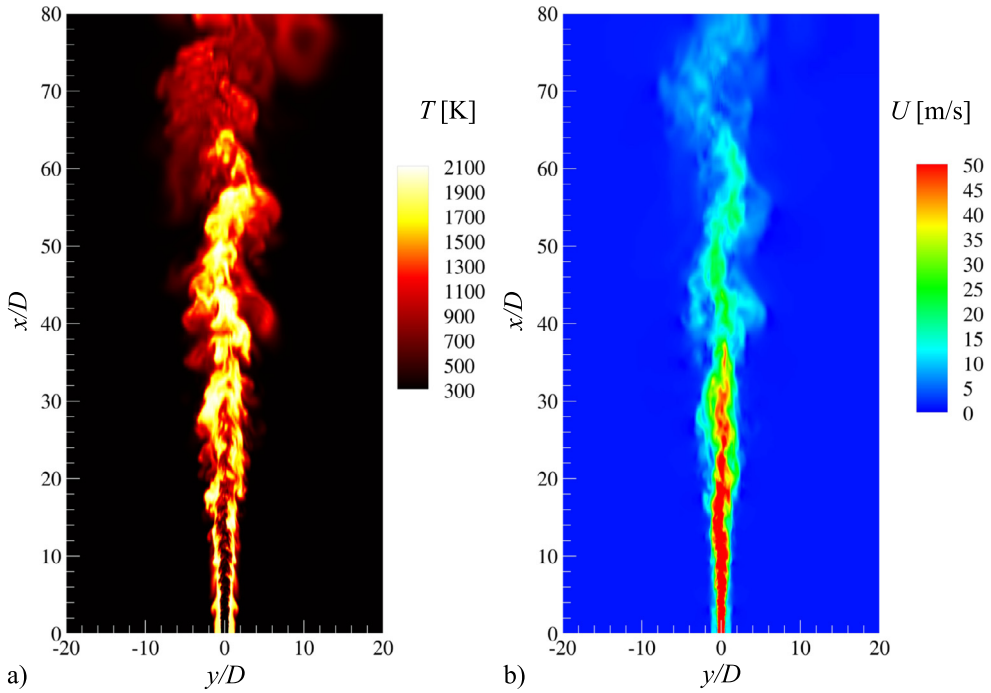

Fig. 5. a) Instantaneous temperature field simulated with fine mesh, and b) instantaneous streamwise velocity field computed with fine mesh.

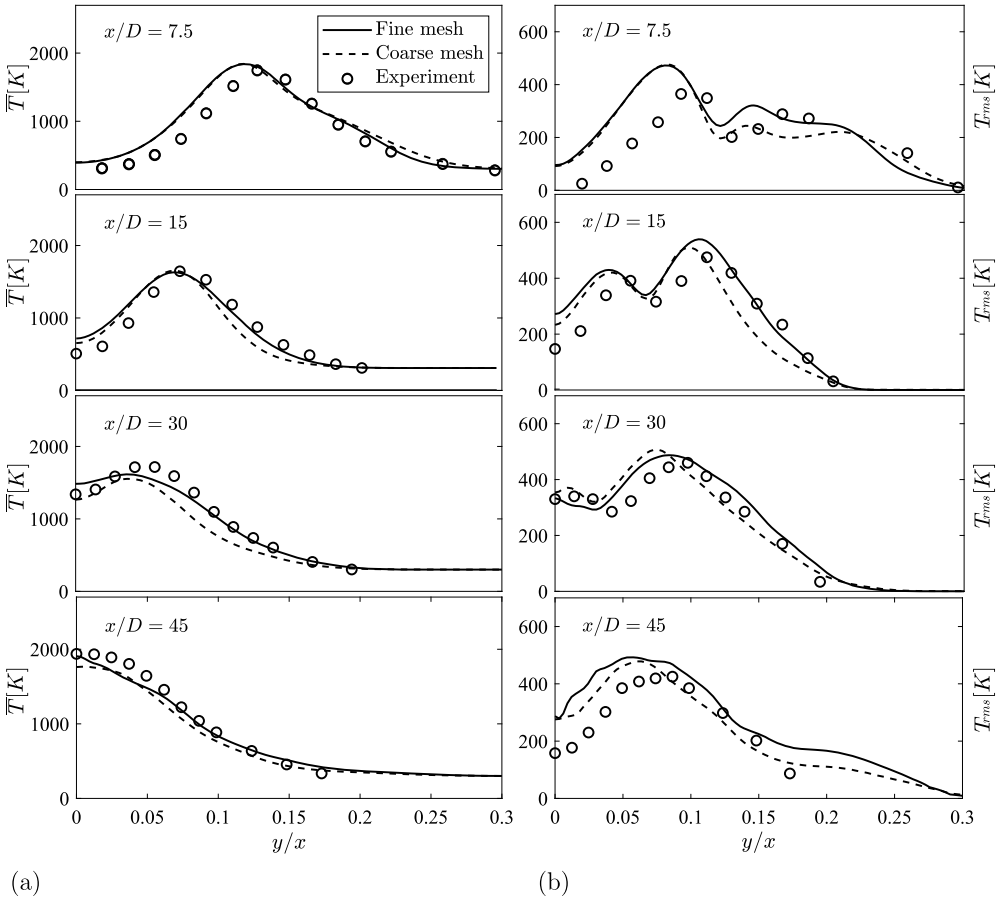

Fig. 6. Comparison of predicted and measured time-averaged (a) and root-mean-square (b) temperature. Legend: solid line–results on fine mesh; dashed line–results on coarse mesh; and circle–experimental data. From top to bottom four rows correspond to the measurement sites of $x/D = 7.5$, $x/D = 15$, $x/D = 30$, and $x/D = 45$, respectively.

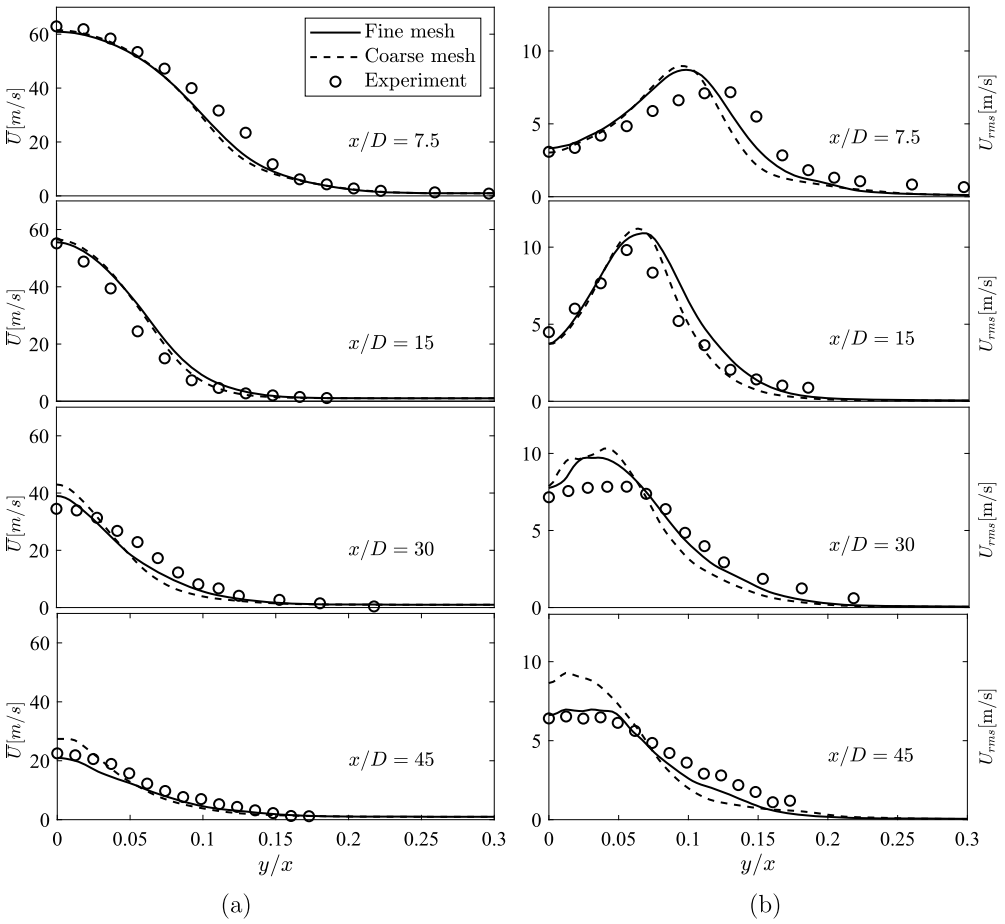

Fig. 7. Comparison of predicted and measured time-averaged (a) and root-mean-square (b) axial velocity. Legend: solid line–results on fine mesh; dashed line–results on coarse mesh; and circle–experimental data. From top to bottom four rows correspond to the measurement sites of $x/D = 7.5$, $x/D = 15$, $x/D = 30$, and $x/D = 45$, respectively.

hibits small overprediction with regard to the experimental results. Similar behaviors of LES solutions are also found in previous studies of Renzo et al. [44], Nik et al. [45] and Yang et al. [46]. The discrepancy in the LES results between two sets of meshes is unnoticeable at $x/D = 7.5$ and $x/D = 15$. However, at the downstream location ($x/D = 30$ and $x/D = 45$), the refined results show better agreement with the experimental data compared to those obtained on the coarse mesh. As for the temperature rms, the peaks of T_{rms} obtained from LES are also shift toward the centerline, similar to the time-averaged temperature profile. The overpredictions of T_{rms} are observed at the locations of $x/D = 7.5$, $x/D = 15$, and $x/D = 45$. Similar issues also exist in previous studies [18,47]. Nevertheless, the largest model errors appear close to jet inlet. This implies that the error source may be the turbulent inflow for which the scalar fluctuations are not accurately modeled. In addition, with regard to the grid sensitivity, the refined case offers better T_{rms} predictions at the outer region, especially at $x/D = 7.5$ and $x/D = 15$ locations.

Fig. 7 shows the radial profiles of the time-average and root-mean-square of the streamwise velocity obtained both from the LES calculations and the experimental measurements. As we can see, the LES predictions have very good agreement with the experimental data. For the mean velocity profile, the descending trends along both the axial and radial directions are well captured by the LES. The results obtained on the fine mesh show marginal improvement compared to those on the coarse mesh. For the velocity rms in Fig. 7(a), a single-peak profile is observed, which is different from the temperature rms in Fig. 6(b). The LES solutions of velocity rms show some discrepancies from the experimental measurements: the predicted peak location is closer to the centerline near the inlet and certain overshoots appear at the downstream locations. It is worth noting that these model errors are also found in previous studies [48]. In their study, Jones and Prasad [48] employed a Eulerian stochastic field method to address the flame-turbulence interaction which should have higher fidelity, but the same model issue persists. This finding implies that the major error source is likely to be the subgrid-scale model which does not introduce sufficient dissipations locally. The overshoot of velocity rms was also found in the study of Xing et al. [6], particularly in the range from $x/D = 15$ to 60. As for the grid sensitivity, it is obvious that the refined case provides considerably better prediction of velocity rms, which is mostly visible at the measurement site $x/D = 45$.

Fig. 8 shows the instantaneous profiles of the mass fractions of the major reaction products, namely H_2O and CO_2, and the intermediate species, including H_2 and CO. As shown, the profiles of intermediate species are much shorter as the combustion has already approached completeness at about $x/D = 40$. Downstream from there the flow field turns to be a pure mixing mode between hot products and ambient coflow air. Profiles for major species coincide with the temperature field displayed in Fig. 5. Fig. 9 shows the radial profiles of the time-averaged mass fractions of H_2O, CO_2, CO and H_2. As we can see, the LES results compare well with the experimental measurements. The refined case offers more accurate predictions for H_2O and CO_2 at the location of $x/D = 15$ and for H_2 and CO at the location of $x/D = 45$. It is worth noting that the overprediction of H_2 and CO near the centerline at $x/D = 15$ is a systematic model error which has been exhibited in previous stud-

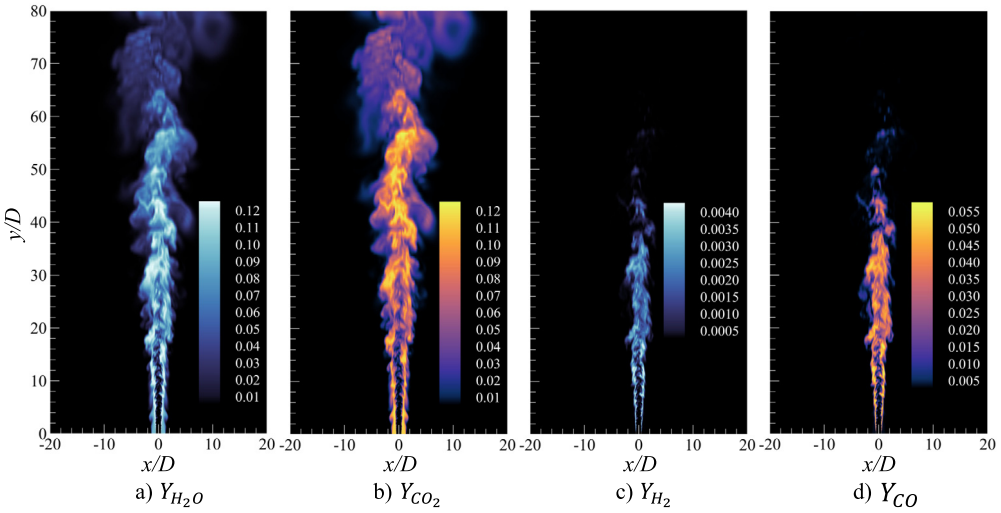

Fig. 8. Instantaneous snapshots of the mass fractions of H_2O (a), CO_2 (b), H_2 (c) and CO (d).

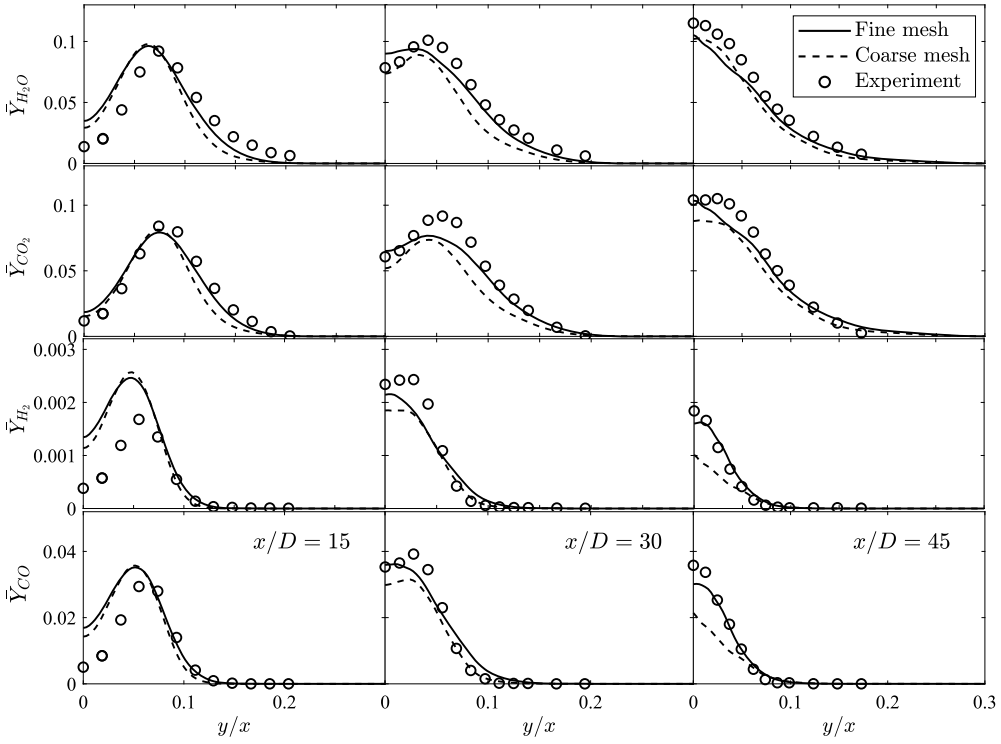

Fig. 9. Comparison of predicted and measured time-averaged mass fractions of H_2O, CO_2, H_2, and CO along radial direction at different measurement sites. Legend: solid line–results on fine mesh; dashed line–results on coarse mesh; and circle–experimental data.

ies [18,47], and it can be attributed to the overprediction of fuel consumption in the rich part of the flame [18]. The overall solution accuracy is comparable to that in the recent study [47] which is equipped with a more sophisticated PDF closure model.

Fig. 10 shows the radial profiles of the rms mass fractions of H_2O, CO_2, CO and H_2. As we can see, for the major species, the rms predictions are in very good agreement with the experimental data. Mesh refinement leads to accuracy improvement in the predictions, especially at the outer region of the jet. On the other hand, the rms predictions of Y_{H_2} and Y_{CO} have comparatively larger discrepancies with respect to the experimental data. At the $x/D = 15$ location, the overprediction, exemplified with a spurious peak near the centerline, is observed. Recognize that the overshoot of time-averaged mass fraction is also observed at the same location, which implies an overprediction of turbulence-induced fluctuations locally. This explains the model errors shown in the Fig. 10. The same model error is also found in the studies of Nik et al. [45] and Duan et al. [47]. Meanwhile, at the downstream location, i.e. $x/D = 45$, the rms is underpredicted. With regard to grid sensitivity, the fine grid results do not show any systematic improvement for rms predictions of H_2 and CO.

5. Conclusions

We developed a new CFD solver for combustion LES based on the fully compressible formulation and tabulated chemistry model.

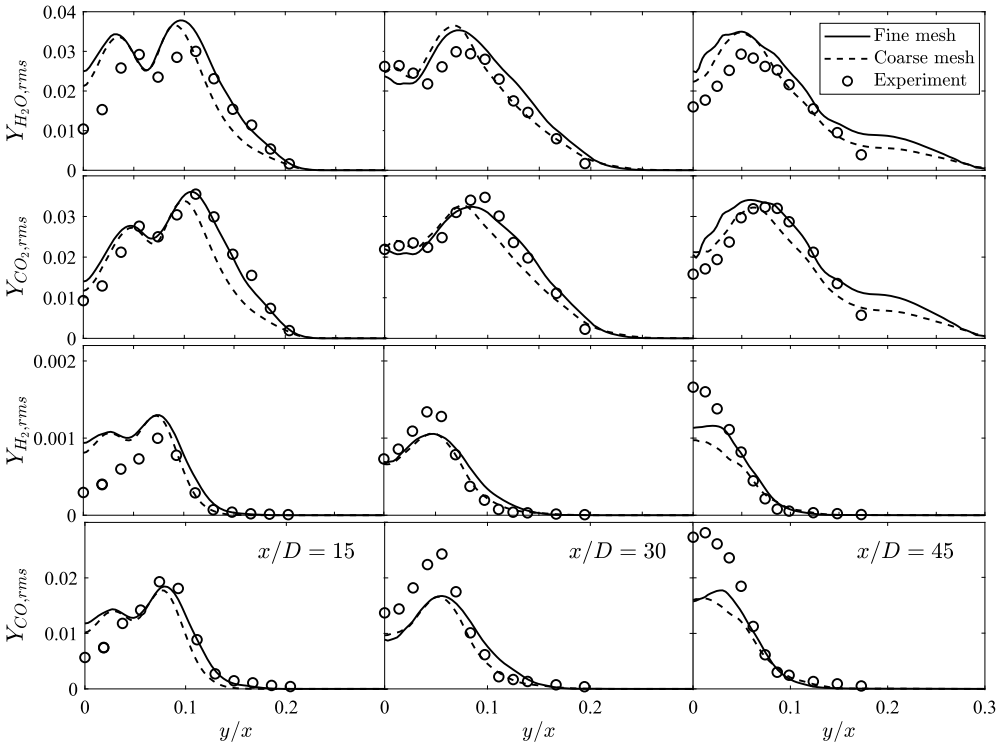

Fig. 10. Comparison of predicted and measured root-mean-square mass fractions of H_2O, CO_2, H_2, and CO along radial direction at different measurement sites. Legend: solid line–results on fine mesh; dashed line–results on coarse mesh; and circle–experimental data.

The solver was first tested in a benchmark case–turbulent scalar mixing, in which two passive scalar diffuses into each other in a decay isotropic turbulent field. Verification was performed by comparing the LES solutions against the filtered DNS data. It was found that the developed LES capability can well reproduce the filtered DNS resolutions at various numerical resolutions.

After the numerical test for non-reactive flows, a validation study on the LES was carried out with consideration of a turbulent jet flame–Sandia Flame D. The LES prediction compared well with the experimental measurements, despite small model errors in the prediction of minor species. Two sets of meshes with 1.4 and 3.9 million cells, respectively, were employed to study the grid sensitivity. It was shown that the finer mesh leads to improved LES predictions of the time-averaged species concentration profiles, especially at the downstream region. In general, it is shown that our combustion LES solver can provide reliable predictions of temperature, species, and flow field. Compared to the flame simulation results obtained using low-Mach solver [18], our predictions of time-averaged quantities have similar accuracy; however, the predictions of fluctuation quantities, such as velocity and temperature root-mean squares, need to be improved. Based on our grid sensitivity study, the error behaviors are independent of mesh resolution and thereby the source of errors is most likely from the subgrid-scale model. In the future, we will investigate the effect of subgrid-scale model on prediction accuracy and implement more sophisticated modeling techniques.

Declaration of competing interest

The authors declare that they have no known competing financial interests or personal relationships that could have appeared to influence the work reported in this paper.

Acknowledgement

This work is supported by the NSFC Basic Science Center Program for “Multiscale Problems in Nonlinear Mechanics” (No. 11988102). YL would like to acknowledge the startup support from the Chinese Academy of Sciences.

Appendix A. Solver validation for high-speed flows

Here an additional validation study is supplemented to verify the solver accuracy for simulations of supersonic flows. We consider a supersonic flow-past-circular-cylinder configuration which was commonly used for code/solver validations [49–51]. A freestream flow with a Mach number of $Ma = 3.5$ is issued into a two-dimensional rectangular channel as shown in Fig. 11(a). The top and bottom boundaries are prescribed as inviscid walls. A circular cylinder with a diameter of D is placed $10D$ downstream from the domain inlet. The domain is $40D$ long in axial direction and $6D$ high in vertical direction. This case contains an unsteady wake flow interacting with reflected shocks and exhibits many interesting features with a very complex flow structure. To capture the shock and wake flow, a locally-refined mesh is employed and as illustrated in Fig. 11(b) the mesh is refined near the cylinder and in the wake region. Total number of cells is about half million.

The instantaneous results are presented in Fig. 12, including the density, temperature and axial-velocity fields. A unique shock pattern is clearly identified, including the leading bow shock and its multiple reflections downstream from the walls. An elongated wake structure is exhibited, along with the unsteadiness induced by the interaction between the wake and the reflected shocks. The results are compared with those obtained using sophisticated numerical methods [49–51], and a good agreement is established.

Quantitative validation was also carried out by examining the shock-induced flow deflection and pressure coefficient. The pres-

Fig. 11. Computational domain and mesh setup.

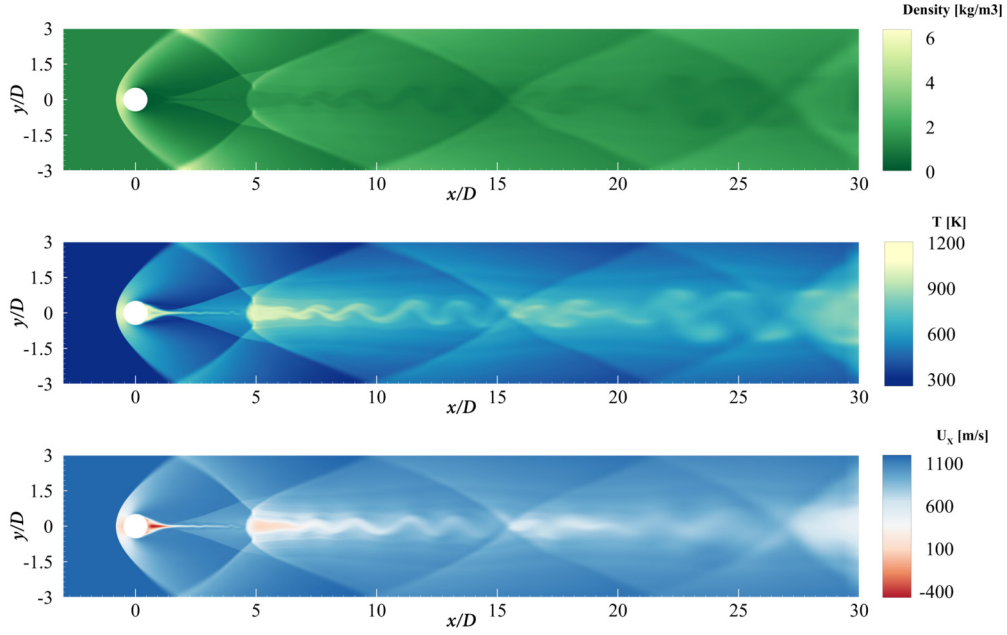

Fig. 12. Instantaneous flow field of the supersonic flow-pass-circular-cylinder case, represented by density, temperature, and axial-velocity from top to bottom.

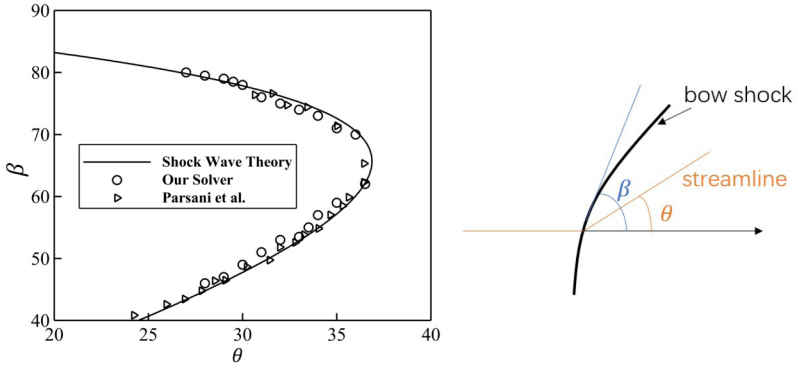

Fig. 13. Relation of shock angle and flow deflection angle, obtained in the present study, by Parsini et al. [51] and from the oblique shock theory.

ence of bow shock modifies the flow direction while leading to a deflection effect. The oblique shock theory provides a useful relation that links the shock angle β with the deflection angle θ, which reads:

$$\tan(\theta) = 2\cot(\beta)\left[\frac{Ma^2\sin^2\beta - 1}{Ma^2(\gamma + \cos(2\beta))} + 2\right]. \tag{20}$$

Both β and θ angles are extracted from the simulation results and compared against the above theoretical relation and the predicted solution of Parsini et al. [51]. As shown in Fig. 13, our result is in good agreement with the two reference solutions. Furthermore, the pressure distribution around the circular cylinder is assessed. The pressure coefficient is plotted as a function of azimuth α with respect to the cylinder center. As shown in Fig. 14, the predicted pressure coefficient by our solver compares well with other existing solutions in literature. Based on the above validation and verification, we show that our solver can accurately capture critical shock structure and flow feature in applications to high-speed flow simulations.

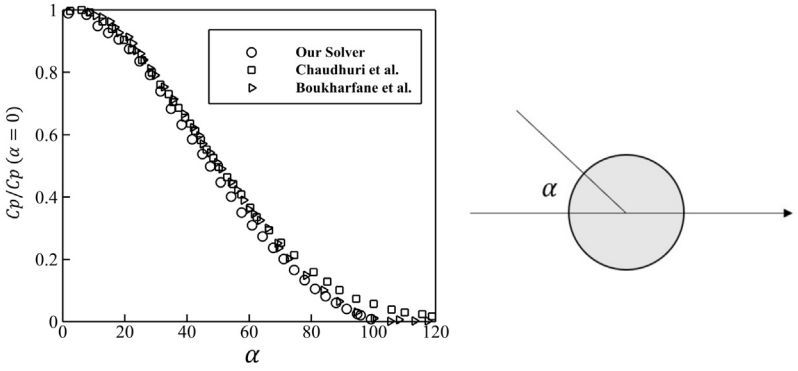

Fig. 14. Pressure coefficient along the cylinder surface, plotted as a function of azimuth α with respect to the cylinder center. Our solution is compared with the results of Chaudhuri et al. [49] and Boukharfane et al. [50].

References

[1] H. Pitsch, Large-eddy simulation of turbulent combustion, Annu. Rev. Fluid Mech. 38 (1) (2006) 453–482, https://doi.org/10.1146/annurev.fluid.38.050304.092133.

[2] X. Han, A.S. Morgans, Simulation of the flame describing function of a turbulent premixed flame using an open-source LES solver, Combust. Flame 162 (5) (2015) 1778–1792, https://doi.org/10.1016/j.combustflame.2014.11.039.

[3] Y. Tang, V. Raman, Large eddy simulation of premixed turbulent combustion using a non-adiabatic, strain-sensitive flamelet approach, Combust. Flame 234 (2021) 111655, https://doi.org/10.1016/j.combustflame.2021.111655.

[4] P. Wang, S.M. Hashemi, H. He, K. Cheng, Investigation of the partially premixed turbulent combustion through the preccinsta burner by large eddy simulation, Aerosp. Sci. Technol. 121 (2022) 107336, https://doi.org/10.1016/j.ast.2022.107336.

[5] L. Xu, G. Zhang, G. Wang, Z. Feng, X. Tian, L. Li, F. Qi, Effects of acoustic liner on thermoacoustic instabilities in a premixed swirl combustor, Aerosp. Sci. Technol. 118 (2021) 107070, https://doi.org/10.1016/j.ast.2021.107070.

[6] Y. Xing, T. Zhang, Z. Tian, J. Li, Y. Yan, Large eddy simulation of a turbulent non-premixed flame based on the flamelet-generated manifolds approach and a reduced mechanism verification, Aerosp. Sci. Technol. 105 (2020) 105952, https://doi.org/10.1016/j.ast.2020.105952.

[7] G. Zhao, J. Du, H. Yang, T. Tang, M. Sun, Effects of injection on flame flashback in supersonic crossflow, Aerosp. Sci. Technol. 120 (2022) 107226, https://doi.org/10.1016/j.ast.2021.107226.

[8] N. Peters, Laminar diffusion flamelet models in non-premixed turbulent combustion, Prog. Energy Combust. Sci. 10 (3) (1984) 319–339, https://doi.org/10.1016/0360-1285(84)90114-X.

[9] T.D. Butler, P.J. O'Rourke, A numerical method for two dimensional unsteady reacting flows, Symp., Int., Combust. 16 (1) (1977) 1503–1515, https://doi.org/10.1016/S0082-0784(77)80432-3.

[10] S. Pope, Computations of turbulent combustion: progress and challenges, Symp., Int., Combust. 23 (1) (1991) 591–612, https://doi.org/10.1016/S0082-0784(06)80307-3.

[11] F. Gao, E.E. O'Brien, A large-eddy simulation scheme for turbulent reacting flows, Phys. Fluids A, Fluid Dyn. 5 (6) (1993) 1282–1284, https://doi.org/10.1063/1.858617.

[12] P.J. Colucci, F.A. Jaberi, P. Givi, S.B. Pope, Filtered density function for large eddy simulation of turbulent reacting flows, Phys. Fluids 10 (2) (1998) 499–515, https://doi.org/10.1063/1.869537.

[13] A.Y. Klimenko, Multicomponent diffusion of various admixtures in turbulent flow, Fluid Dyn. 25 (3) (1990) 327–334, https://doi.org/10.1007/BF01049811.

[14] R.W. Bilger, Conditional moment closure for turbulent reacting flow, Phys. Fluids A, Fluid Dyn. 5 (2) (1993) 436–444, https://doi.org/10.1063/1.858867.

[15] C.D. Pierce, P. Moin, Progress-variable approach for large-eddy simulation of non-premixed turbulent combustion, J. Fluid Mech. 504 (504) (2004) 73–97, https://doi.org/10.1017/S0022112004008213.

[16] H. Pitsch, M. Ihme, An unsteady/flamelet progress variable method for LES of nonpremixed turbulent combustion, in: Proceedings of AIAA Aerospace Sciences Meeting & Exhibit AIAA, 2005.

[17] M. Ihme, H. Pitsch, Prediction of extinction and reignition in nonpremixed turbulent flames using a flamelet/progress variable model 1. A priori study and presumed PDF closure, Combust. Flame 155 (1–2) (2008) 70–89, https://doi.org/10.1016/j.combustflame.2008.04.001.

[18] M. Ihme, H. Pitsch, Prediction of extinction and reignition in nonpremixed turbulent flames using a flamelet/progress variable model 2. Application in LES of Sandia flames D and E, Combust. Flame 155 (1–2) (2008) 90–107, https://doi.org/10.1016/j.combustflame.2008.04.015.

[19] M. Oevermann, Numerical investigation of turbulent hydrogen combustion in a SCRAMJET using flamelet modeling, Aerosp. Sci. Technol. 4 (7) (2000) 463–480, https://doi.org/10.1016/S1270-9638(00)01070-1.

[20] G. Zhao, J. Du, M. Liu, H. Wang, M. Sun, Numerical investigation of the scale effects of the flame flashback phenomenon in scramjet combustors, Aerosp. Sci. Technol. 119 (2021) 107165, https://doi.org/10.1016/j.ast.2021.107165.

[21] W. Yao, H. Liu, L. Xue, Y. Xiao, Performance analysis of a strut-aided hypersonic scramjet by full-scale iddes modeling, Aerosp. Sci. Technol. 117 (2021) 106941, https://doi.org/10.1016/j.ast.2021.106941.

[22] G. Xu, P. Liu, W. Ao, Z. Wang, B. Jin, Numerical investigation of thermoacoustic instability caused by small disturbance in a solid rocket motor, Aerosp. Sci. Technol. 113 (2021) 106678, https://doi.org/10.1016/j.ast.2021.106678.

[23] A. Saghafian, V.E. Terrapon, H. Pitsch, An efficient flamelet-based combustion model for compressible flows, Combust. Flame 162 (3) (2015) 652–667, https://doi.org/10.1016/j.combustflame.2014.08.007.

[24] Z. Gao, C. Jiang, C.H. Lee, Representative interactive flamelet model and flamelet/progress variable model for supersonic combustion flows, Proc. Combust. Inst. 36 (2) (2017) 2937–2946, https://doi.org/10.1016/j.proci.2016.06.184.

[25] F. Ladeinde, Z. Lou, W. Li, The effects of pressure treatment on the flamelet modeling of supersonic combustion, Combust. Flame 204 (2019) 414–429, https://doi.org/10.1016/j.combustflame.2019.03.030.

[26] F. Shan, D. Zhang, L. Hou, H. Fang, H. Zhang, J. Zhang, An improved flamelet/progress variable modeling for supersonic combustion, Int. J. Hydrog. Energy 46 (5) (2021) 4485–4495, https://doi.org/10.1016/j.ijhydene.2020.10.225.

[27] A. Vreman, An eddy-viscosity subgrid-scale model for turbulent shear flow: algebraic theory and applications, Phys. Fluids 16 (10) (2004) 3670–3681.

[28] N. Peters, Turbulent Combustion, Cambridge Monographs on Mechanics, Cambridge University Press, 2000.

[29] A. Saghafian, High-fidelity simulations and modeling of compressible reacting flows, Ph.D. thesis, Stanford University, 2014.

[30] H. Pitsch, Flamemaster v3.3.10: a C++ computer program for 0D combustion and 1D laminar flame calculations, http://www.itv.rwth-aachen.de/en/downloads/flamemaster, 1998.

[31] Y. Lv, Development of a nonconservative discontinuous Galerkin formulation for simulations of unsteady and turbulent flows, Int. J. Numer. Methods Fluids 92 (5) (2020) 325–346.

[32] T. Barth, P. Frederickson, Higher order solution of the Euler equations on unstructured grids using quadratic reconstruction, in: 28th Aerospace Sciences Meeting, 1990, p. 13.

[33] M.-S. Liou, A sequel to Ausm: Ausm+, J. Comput. Phys. 129 (2) (1996) 364–382.

[34] Y. Lv, M. Ihme, Discontinuous Galerkin method for multicomponent chemically reacting flows and combustion, J. Comput. Phys. 270 (2014) 105–137.

[35] Y. Lv, M. Ihme, Computational analysis of re-ignition and re-initiation mechanisms of quenched detonation waves behind a backward facing step, Proc. Combust. Inst. 35 (2) (2015) 1963–1972.

[36] Y. Lv, P.C. Ma, M. Ihme, On underresolved simulations of compressible turbulence using an entropy-bounded DG method: solution stabilization, scheme optimization, and benchmark against a finite-volume solver, Comput. Fluids 161 (2018) 89–106.

[37] V. Eswaran, S. Pope, Direct numerical simulations of the turbulent mixing of a passive scalar, Phys. Fluids 31 (3) (1988) 506–520.

[38] R. Barlow, Website for the International Workshop on Measurement and Computation of Turbulent Non-premixed Flames (TNF), 1996.

[39] R. Barlow, J. Frank, Effects of turbulence on species mass fractions in methane/air jet flames, Symp., Int., Combust. 27 (1) (1998) 1087–1095, https://doi.org/10.1016/S0082-0784(98)80510-9.

[40] C. Schneider, A. Dreizler, J. Janicka, E. Hassel, Flow field measurements of stable and locally extinguishing hydrocarbon-fuelled jet flames, Combust. Flame 135 (1–2) (2003) 185–190, https://doi.org/10.1016/S0010-2180(03)00150-0.

[41] T.S. Lund, X. Wu, K.D. Squires, Generation of turbulent inflow data for spatially-developing boundary layer simulations, J. Comput. Phys. 140 (2) (1998) 233–258, https://doi.org/10.1006/jcph.1998.5882.
[42] M. Klein, A. Sadiki, J. Janicka, A digital filter based generation of inflow data for spatially developing direct numerical or large eddy simulations, J. Comput. Phys. 186 (2) (2003) 652–665, https://doi.org/10.1016/S0021-9991(03)00090-1.
[43] Z. Xie, I.P. Castro, Efficient generation of inflow conditions for large eddy simulation of street-scale flows, Flow Turbul. Combust. 81 (3) (2008) 449–470, https://doi.org/10.1007/s10494-008-9151-5.
[44] M.D. Renzo, A. Coclite, M.D.D. Tullio, P.D. Palma, G. Pascazio, LES of the Sandia Flame D using an FPV combustion model, Energy Proc. 82 (2015) 402–409, https://doi.org/10.1016/j.egypro.2015.11.824.
[45] M.B. Nik, S.L. Yilmaz, P. Givi, M.R.H. Sheikhi, S.B. Pope, Simulation of Sandia flame D using velocity-scalar filtered density function, AIAA J. 48 (7) (2010) 1513–1522, https://doi.org/10.2514/1.J050154.
[46] S. Yang, X. Wang, H. Huo, W. Sun, V. Yang, An efficient finite-rate chemistry model for a preconditioned compressible flow solver and its comparison with the flamelet/progress-variable model, Combust. Flame 210 (2019) 172–182.
[47] Y. Duan, Z. Xia, L. Ma, Z. Luo, X. Huang, X. Deng, LES of the Sandia flame series D-F using the Eulerian stochastic field method coupled with tabulated chemistry, Chin. J. Aeronaut. 33 (1) (2020) 116–133, https://doi.org/10.1016/j.cja.2019.09.022.
[48] W. Jones, V. Prasad, Large Eddy Simulation of the Sandia Flame Series (D–F) using the Eulerian stochastic field method, Combust. Flame 157 (9) (2010) 1621–1636.
[49] A. Chaudhuri, A. Hadjadj, A. Chinnayya, On the use of immersed boundary methods for shock/obstacle interactions, J. Comput. Phys. 230 (5) (2011) 1731–1748.
[50] R. Boukharfane, F.H.E. Ribeiro, Z. Bouali, A. Mura, A combined ghost-point-forcing/direct-forcing immersed boundary method (ibm) for compressible flow simulations, Comput. Fluids 162 (2018) 91–112.
[51] M. Parsani, R. Boukharfane, I.R. Nolasco, D.C.D.R. Fernández, S. Zampini, B. Hadri, L. Dalcin, High-order accurate entropy-stable discontinuous collocated Galerkin methods with the summation-by-parts property for compressible cfd frameworks: scalable ssdc algorithms and flow solver, J. Comput. Phys. 424 (2021) 109844.